Fast Acoustic Wave Sparsely Activated Localization Microscopy: Ultrasound Super-Resolution Using Plane-Wave Activation of Nanodroplets

Ge Zhang, Sevan Harput, Hanyu Hu, Kirsten Christensen-Jeffries, Jiaqi Zhu, Jemma Brown, Chee Hau Leow, Robert J. Eckersley, Christopher Dunsby, and Meng-Xing Tang, *Senior Member, IEEE*

Abstract—Localization-based ultrasound super-resolution imaging using microbubble contrast agents and phase-change nanodroplets has been developed to visualize microvascular structures beyond the diffraction limit. However, the long data acquisition time makes the clinical translation more challenging. In this study, fast acoustic wave sparsely activated localization microscopy (fast-AWSALM) was developed to achieve super-resolved frames with subsecond temporal resolution, by using low-boiling-point octafluoropropane nanodroplets and high frame rate plane waves for activation, destruction, as well as imaging. Fast-AWSALM was demonstrated on an *in vitro* microvascular phantom to super-resolve structures that could not be resolved by conventional B-mode imaging. The effects of the temperature and mechanical index on fast-AWSALM were investigated. The experimental results show that subwavelength microstructures as small as 190 μm were resolvable in 200 ms with plane-wave transmission at a center frequency of 3.5 MHz and a pulse repetition frequency of 5000 Hz. This is about a 3.5-fold reduction in point spread function full-width-half-maximum compared to that measured in the conventional B-mode, and two orders of magnitude faster than the recently reported AWSALM under a nonflow/very slow flow situations and other localization-based methods. Just as in AWSALM, fast-AWSALM does not require flow, as is required by current microbubble-based ultrasound super-resolution techniques. In conclusion, this study shows the promise of fast-AWSALM, a super-resolution ultrasound technique using nanodroplets, which can generate super-resolution images in milliseconds and does not require flow.

Index Terms—Acoustic droplet vaporization, octafluoropropane (OFP) nanodroplet, super-localization, super-resolution imaging, ultrafast.

I. Introduction

LOCALIZATION-BASED ultrasound super-resolution imaging techniques are rapidly evolving. Early studies reported that the detection of isolated microbubble signals in the radio frequency (RF) domain [1], [2] or image domain [3], [4] can be used to generate super-resolution imaging *in vitro*. Two recent studies have shown the capability of using these techniques with microbubbles *in vivo* to super-resolve the microvessels and also obtain flow information [5], [6]. Subsequently, a number of papers have been published which improve and extend the microbubble-assisted super-resolution imaging technique in different ways, including signal filtering and detection [7], [8], choice of localization method [9], motion correction [10], signal tracking [11], and 3-D imaging [12]–[14].

Current localization-based super-resolution imaging techniques using microbubbles rely on sufficient flow and most require a low bubble concentration to provide spatially isolated localizations. Thus, longer acquisition time is required for sampling microbubbles in small vessels as they are very sparsely distributed at the capillary level and flow slowly in such vessels.

Nanodroplets, as ultrasound contrast agents, have three main advantages over microbubbles [15]. First, the nanosize of nanodroplets potentially allows extravasation into cancerous tissue due to its leaky vasculature and enhanced permeability and retention effects. Second, it has been found that nanodroplets can last longer during *in vivo* circulation than microbubbles [16]. Third, the nanodroplets can be selectively activated, both spatially and temporally, to provide an ultrasound contrast signal [17]. This potentially provides more flexibility during the ultrasound scanning.

Recent studies have reported ultrasound super-resolution imaging using low- (boiling point = −2 °C) [18], [19] and high- (boiling point = 56 °C) [20], [21] boiling-point perfluorocarbon nanodroplets. For the super-resolution imaging technique using high-boiling-point nanodroplets, optical activation via pulsed laser illumination was required to perform the super-resolution imaging, thus restricting its penetration depth to regions that can be illuminated optically. Furthermore, as the pulse repetition frequency of laser activation was 10 Hz, longer acquisition time is required in comparison to the fast ultrasound imaging methods with a pulse

repetition frequency over thousands of Hertz. The "acoustic wave sparsely activated localization microscopy (AWSALM)," developed by our group, has shown that the use of low-boiling-point perfluorocarbon nanodroplets (with much lower activation threshold than high-boiling-point nanodroplets) can be acoustically activated and deactivated by diagnostic ultrasound pulses to perform ultrasound super-resolution imaging in deep tissue. Unlike microbubble-based super-resolution techniques, AWSALM does not require flow, nor does it require a low concentration of the contrast agent.

Microbubble-based ultrasound super-resolution technique requires long data acquisition time, which together with the motion during data acquisition makes it challenging for clinical use. AWSALM requires different ultrasound transmissions for droplets activation/deactivation and imaging, limiting the temporal resolution achievable.

In this study, we develop fast-AWSALM and demonstrate that a high concentration of low-boiling-point octafluoropropane (OFP) nanodroplets can be simultaneously imaged, activated, and deactivated by high-frame-rate plane-wave pulses at an intermediate acoustic amplitude to perform ultrasound super-resolution imaging on the time scale of hundreds of milliseconds. One of the fundamental distinctions between bubble- and droplet-based super-resolution imaging techniques is that while using bubbles localizations in consequent frames are not independent and they decorrelate with the velocity of flow, which is slow in the capillaries even if high concentrations of bubbles are present. However, with droplets being activated and deactivated at the same rate with ultrasound pulse repetition frequency, new localizations can be accumulated as quickly as the imaging pulses are transmitted. This fast and controlled activation and deactivation of nanodroplets make it possible to achieve a much faster super-resolution imaging.

II. Materials and Methods

A. Preparation of OFP Microbubbles and Nanodroplets

Nanodroplet preparation was adapted from previously described methods [22]–[24]. Briefly, a lipid colloid was generated by dissolving a 9:1 molar ratio of 1,2-dipalmitoyl-sn-glycero-3-phosphocholine (DPPC) and 1,2-distearoyl-sn-glycero-3-phosphoethanolamine-N-[amino(polyethylene glycol)-2000] (DSPE-PEG-2000) into a solution of phosphate-buffered saline (PBS), propylene glycol, and glycerol (16:3:1, v:v) to achieve a total lipid concentration of 1 mg/mL. All the lipids described above were purchased from Avanti Polar Lipids, Inc., Alabaster, AL, USA. A volume of 1 mL of lipid solution was added to a 2-mL glass vial. The headspace of the vial was filled with OFP gas (FluoroMed, Round Rock, TX, USA) via an inlet needle along with a vent needle. The 60 s of mechanical agitation at 4000 r/min was applied using a bubble shaker (Vialmix, N. Billerica, MA, USA) to produce the stable OFP microbubbles.

In order to condense microbubbles into nanodroplets, the headspace of the vial was pressurized according to the previously described methods [25]. The vial of microbubble solution was immersed in an ice-salt bath (about -10 °C) for 3 min followed by pressurization (85–130 lbf/in^2) with ambient air into the vial septum for the condensation.
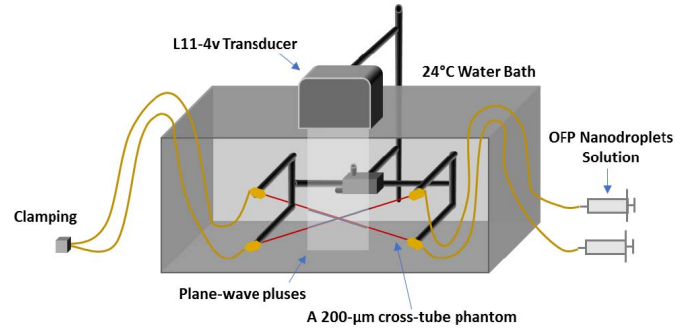

Fig. 1. Schematic showing the experimental setup (not to scale).

B. Characterization of OFP Microbubbles and Nanodroplets

The size and concentration of OFP nanodroplets was measured by NanoSight NS300 (Malvern Instruments Ltd., Malvern, U.K.) via nanoparticle tracking analysis. The nanodroplet solution was diluted 1000-fold in degassed and deionized water. Three samples were prepared and three measurements were performed for each sample. Nine measurements in total were performed to obtain the mean values of diameter and concentration of the nanodroplet solution. The precursor OFP microbubbles were sized and counted using the approach detailed in [26]. A diluted microbubble solution was introduced into the counting chamber of the hemocytometer. Images were acquired from a microscope system (Nikon Instruments Inc., Melville, NY, USA) and counting and sizing were performed in a fully automatic and bespoke MATLAB algorithm. Three measurements in total were performed to obtain the mean values of the diameter of the OFP microbubble solution.

C. Experimental Setup

A crossed-tube phantom was fixed and immersed in a water tank. A schematic showing the experimental setup is illustrated in Fig. 1. The crossed-tube phantom was made of two 200-μm-cellulose tubes (Hemophan, Membrana). The tube is a thin-walled cellulose capillary tube of internal diameter of 200 ± 15 μm with a wall thickness of 8 ± 1 μm in the dry state (specifications provided by the manufacturer). An L11-4v transducer equipped with ultrasound research platform (Verasonics Vantage 128, Kirkland, WA, USA) was held 20 mm above the center of the crossed-tubes. OFP droplets were tested as a function of temperature (18 °C, 24 °C, 30 °C, and 37 °C) and tested as a function of mechanical index (MI) (0.55, 0.66, and 0.76) at 24 °C to determine the optimal experimental conditions. Equal concentrations of 1:9 water-diluted nanodroplet and microbubble solutions ($\sim 3.3 \times 10^8$ agents/mL) were prepared, respectively, in two beakers. The solution was magnetically stirred in the beaker before being transferred into the syringes. The experiments were repeated at different temperatures and MIs.

D. Characterization of Imaging System

The ultrasound imaging system was characterized by measuring the diffraction limited resolution through system point spread function (PSF) and localization precision. A 50-μm-diameter tube was fixed horizontally in a water tank to

imitate a point scatterer [5]. This was performed at depths of between 1.5 and 2.5 cm from the transducer surface to test the changes in PSF over the imaging depth. The resolution of the ultrasound imaging system was measured as the mean value of full-width half-maximum (FWHM) over 100 frames in the lateral and axial directions. The localization precision was measured to be the standard deviation of the localized center of mass over 100 frames. A single average PSF was used for the super-resolution processing at all depths.

E. Data Acquisition and Processing

A customized continuous "Activation/Imaging" pulse sequence was developed and implemented on the ultrasound research platform with an L11-4 linear array probe. A sequence of 1-cycle, 3.5-MHz single-angle plane-wave pulses was transmitted at a MI of 0.76 in order to simultaneously activate, deactivate, and image the OFP nanodroplet population. All 128 elements were used to transmit and receive signals. The corresponding spatial and temporal peak negative pressure was 1.42 MPa. The pressure field of the plane wave was calibrated using a 0.2-mm needle hydrophone (Precision Acoustics, Dorchester, U.K.). No transmit apodization was applied on the acquisition sequence. An optical image of the crossed-tube phantom was taken by a charge coupled devices (CCD) camera.

Thousand images were acquired during a 200-ms period at a frame rate of 5000 frames/s for each experiment. The received RF signals were beamformed using delay-and-sum (DAS) [27]. Singular value decomposition (SVD) was used to remove background noncontrast agent signal [8]. The SVD thresholds were automatically determined by the point with the largest second derivative of energy with respect to singular value order curves.

All the ultrasound image frames were envelope detected after SVD processing. Super-localization processing was performed on each ultrasound image after setting an image pixel value threshold to reject the noise and detect potential activated or deactivated droplet signals. Each observed PSF was compared with a calibration PSF according to their area (A), intensity (I), and shape/eccentricity (E). These parameters were used to discard potential nonmicrobubble echoes and noises. All the observed PSFs with the corresponding three attributes were summarized into three matrices. All the values were normalized in each matrix. A filtering threshold was set in order to discard the larger ($A > 0.46$), brighter ($I > 0.21$), and misshaped ($E < 0.66$) PSF. The locations of isolated signals were calculated by the "centroid" method [5]. The centroid of each localized signal was computed by calculating the intensity-weighted center of mass. All the localizations from all the imaging frames were assembled into the final super-resolution image.

III. RESULTS

A. Characterization of OFP Microbubbles and Nanodroplets

The normalized size distribution of the OFP microbubbles was measured using an optical microscopy approach detailed in [26] and the result was illustrated in Fig. 2(a). The mean microbubble diameter was 1.12 ± 0.36 μm and the mean
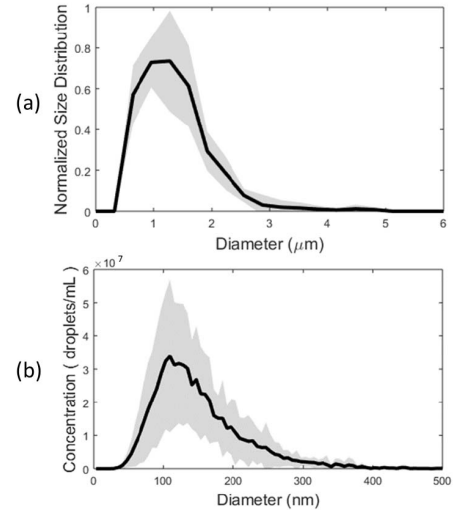

Fig. 2. (a) Size characterization of the OFP microbubbles. The curve and its corresponding shaded error bar represent the mean and standard deviation of three repeated measurements, respectively. (b) Size and concentration characterization of the OFP nanodroplets measured using NanoSight NS300. The curve and its corresponding shaded error bar represent the mean and standard deviation of nine repeated measurements, respectively.
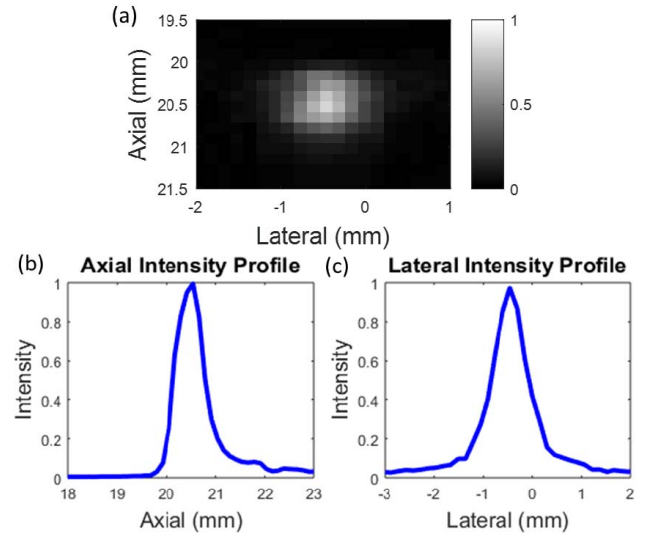

Fig. 3. Calibration of ultrasound imaging system—Verasonics 128 research platform equipped with an L11-4v probe. (a) Representative frame of the 50-μm-diameter tube across section imaged at a distance of 2 cm, which is the same imaging distance used for the crossed-tube phantom. Measurements of the FWHM in (b) axial and (c) lateral directions, respectively.

microbubble concentration was $(3.4 \pm 0.4) \times 10^9$ bubbles/mL. The OFP nanodroplet size and concentration measurements are illustrated in Fig. 2(b). The mean diameter of the OFP nanodroplets was 153.4 ± 6.9 nm. The concentration of nanodroplets was $(3.3 \pm 0.2) \times 10^9$ droplets/mL.

B. Calibration of Diffraction Limited Resolution

Fig. 3(a) shows an example image of the 50-μm wire cross section at a depth of about 2 cm, which is the same depth used for imaging the center of the crossed-tube phantom. The wire acts as a stationary point scatterer and was used to estimate the actual diffraction limited resolution over the depth ranged from 1.5 to 2.5 cm. All the parameters and conditions were
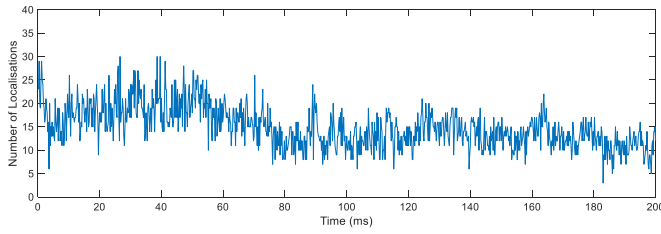
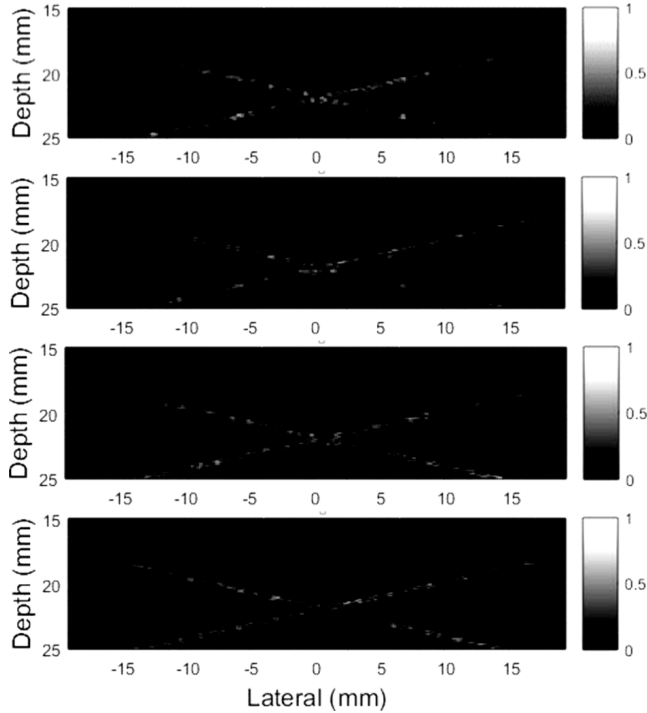Fig. 4. Number of localization events in each frame over 200 ms.

Fig. 5. Representative image frames show the activation of nanodroplets and destruction of microbubble signals over four successive ultrasound image frames.

kept the same as used for imaging the crossed-tube phantom. The mean axial and lateral resolution was measured as the FWHM of 664 and 657 μm, respectively, at a depth of about 2 cm. The localization precision was 20 μm, which was the value used for the later localization processing.

C. Localization of Signals

The average number of localization events is 15 per frame. As can be seen from Fig. 4, 14918 localization events were obtained in total and used to generate the super-resolution image at a temperature of 24 °C and an MI of 0.76.

Fig. 5 shows, over a series of high-pressure plane-wave imaging pulses, the sparse activation of nanodroplets and the destruction of microbubbles signals over time.

D. Quantification of the Number of Localization Events at Different Temperatures

Fig. 6 shows the superlocalization images obtained using the OFP nanodroplets at four different temperatures (18 °C, 24 °C, 30 °C, and 37 °C). Fig. 7 shows the number of localization events obtained at different temperatures. The
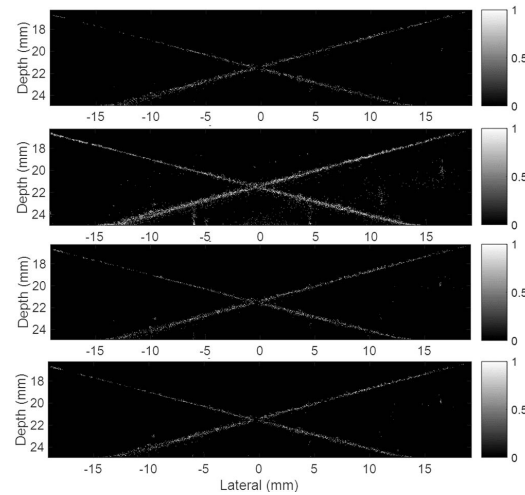
Fig. 6. Final super-localization images at different temperatures (temperature at 18 °C, 24 °C, 30 °C, and 37 °C).
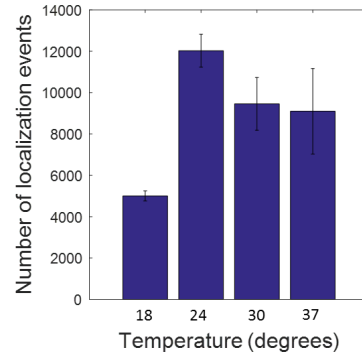
Fig. 7. Number of localization events at different temperatures (temperature at 18 °C, 24 °C, 30 °C, and 37 °C). The experiments were performed for three times to obtain the mean and standard deviation values.

mean and standard deviation values were obtained from three repeated experiments.

E. Quantification of the Number of Localization Events at Different Mechanical Indices

Fig. 8 shows the super-localization images obtained using the OFP nanodroplets at three MIs (MI = 0.55, 0.66, and 0.76). Fig. 9 shows the number of localization events at different MIs. The mean and standard deviation values were obtained by three repeated experiments.

F. Super-Resolution Imaging

Fig. 10 represents the summation of 1000 B-mode, SVD-filtered, and super-localization frames acquired without contrast agents, and with microbubble and nanodroplets, respectively, in the nonflow cross-tube phantom. As can be seen in Fig. 10(d), for the control experiment with water, after SVD filtering, no bubble signals were detected. For the microbubble experiment, after starting acquiring data, most of the bubbles were destroyed by the high MI pulses during the first few frames and insufficient localization events were recorded to generate a proper super-resolution image. For the nanodroplets, they can be continuously activated and deactivated by high-frame-rate plane-wave pulses to
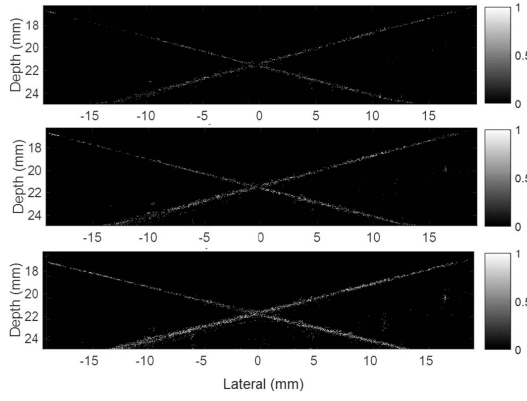
Fig. 8. Final super-localization images at different MIs (MI = 0.55, 0.66, and 0.76).
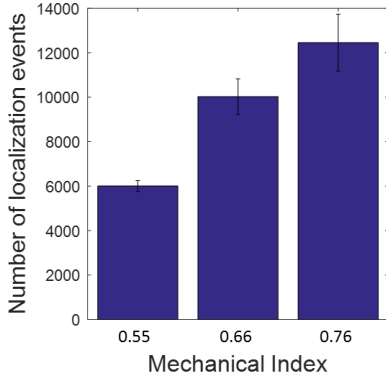

Fig. 9. Final super-localization images at different temperatures (MI = 0.55, 0.66, and 0.76). The experiments were performed for three times to obtain the mean and standard deviation values.

form a super-resolution image from 1000 frames acquired over 200 ms.

G. Resolution Measurement

As can be seen from Fig. 11, the corresponding B-mode, SVD-filtered, and super-resolution images were compared with the optical image. Two regions of interest (ROIs) were selected to measure the FWHM of the B-mode, SVD-filtered, and super-resolution images. In the super-resolution image, it can be seen from the line profile shown in Fig. 11(e) that the two tubes are separated by 210 μm ("peak-to-peak" distance), whereas the two tubes cannot be resolved in B-mode or SVD-filtered images. From Fig. 11(f), it can be seen that the FWHM values are about 190 and 200 μm for the super-resolution image where they are about 690 and 700 μm in the B-mode and SVD-filtered images.

IV. DISCUSSION

This paper presents an *in vitro* demonstration of super-resolution imaging achieved with the timescale of 200 ms using high-frame-rate plane-wave activation of the OFP nanodroplets, called fast-AWSALM. It takes advantage of the high temporal resolution of high-frame-rate plane-wave imaging and the low activation threshold of the OFP nanodroplets to perform super-resolution imaging orders of magnitude faster than previously demonstrated. Another advantage of having a faster imaging technique as proposed in this work

is the ability to reduce the impact of tissue motion. It was demonstrated that tissue motion can be detrimental to ultrasound super-resolution imaging, and motion correction can improve the resolution and fidelity of the super-resolved images [10].

It should be noted that the resolution achieved in this study, 190 μm, is not a limitation of the fast-AWSALM method but a limitation of the phantom available to us (200-μm tube). While the experimental conditions used in this study for comparing droplet- and bubble-based super-resolution approaches are the same, the conditions are not designed for bubble-based approaches. We have previously shown in a similar phantom [3] but with flow and with lower MI that reasonable super-resolution images of the cross-tube phantom can be achieved using microbubbles although it took much longer than the droplet-based approach.

A. Comparison With Existing Localization-Based Super-Resolution Imaging Techniques

The acquisition time of previously demonstrated localization-based super-resolution imaging using microbubbles ranges from 5 s to a few minutes [5], [6], [8], [14].

The AWSALM technique reported previously used separate pulses for imaging and for activation/deactivation of nanodroplets, as the decafluorobutane (DFB) nanodroplets require a relatively high ultrasound amplitude to be activated [18]. Such a high ultrasound amplitude is only achievable at one location at a time through focused transmission. Therefore, it takes time to scan the activating pulses through the whole imaging plane. The previous AWSALM study took 30 s to obtain a super-resolution imaging of the crossed-tube phantom at a frame rate of 100 Hz. However, there should not be a penalty in terms of resolution since the imaging method is the same between AWSALM and fast-AWSALM (i.e., plane wave imaging), and the only difference is that the activation pulse is now also an imaging pulse in fast-AWSALM.

A different formulation of lower boiling-point OFP (boiling point = -37 °C) nanodroplets was used in this study compared with the DFB (boiling point = -2 °C) nanodroplets used in the previous study. Thus, the OFP nanodroplets could be activated by lower MI plane-wave pulses compared with DFB nanodroplets. The focus-wave pulses are not required in this study as the acoustic pressure provided by plane-wave imaging pulses is sufficiently high to activate the OFP nanodroplets. Therefore, the activation of the droplets can be achieved within the imaging plane by a single plane wave, and such activation can then be imaged by the very same activation plane wave. As such plane waves can be transmitted at thousands pulses per second, a significant increase in imaging frame in super-resolution can be achieved. In this case, an imaging acquisition rate of 5000 frames/s frame rate was used, enabling super-resolved image data acquisition in 200 ms, which is orders of magnitude faster than the previous localization-based super-resolution techniques [8].

B. Sparse Activation and Destruction

The principle of fast-AWSALM is that the first plane-wave imaging pulse will sparsely activate a subgroup of the OFP
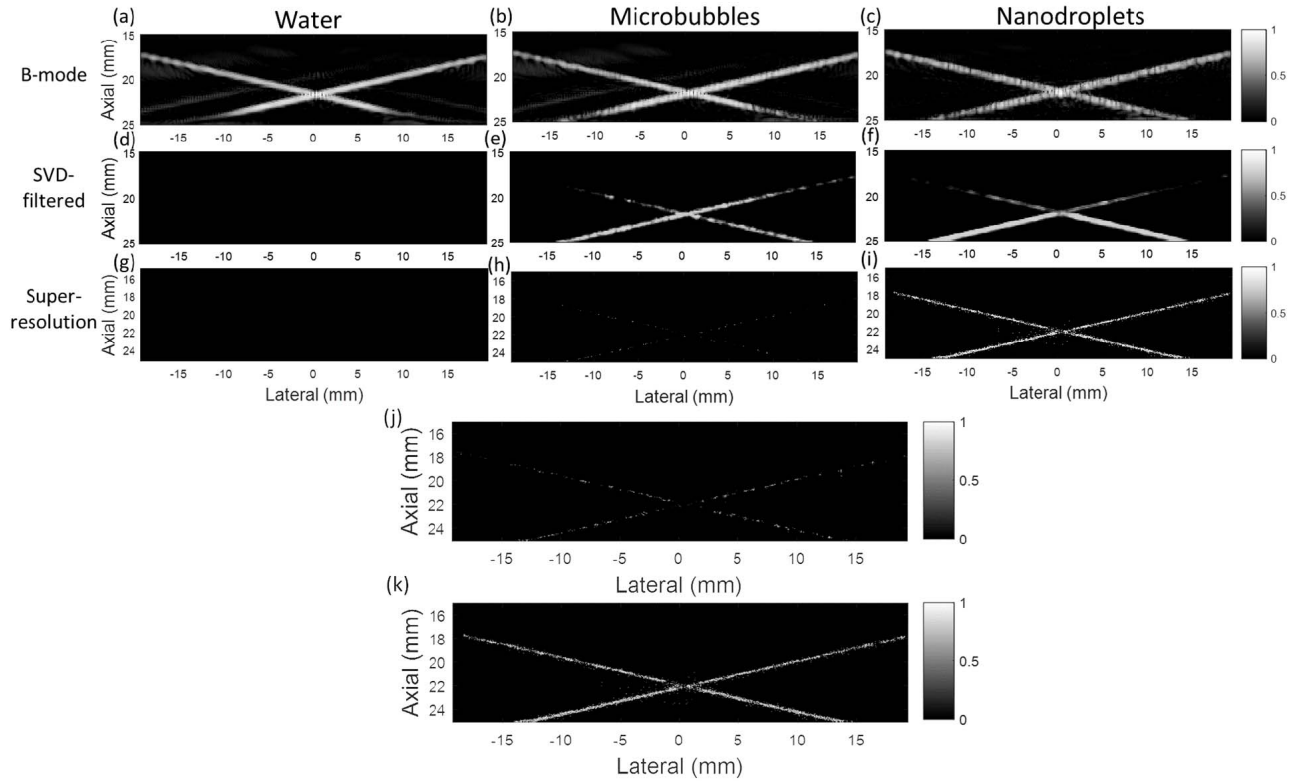
Fig. 10. (a)–(c) Summation of 1000 conventional B-mode images. (d)–(f) Summation of the corresponding SVD-filtered images. (g)–(i) Final super-resolution images for water (a), (d), and (g), microbubble (b), (e), and (h), and nanodroplet (c), (f), and (i) experiments, respectively. (j) and (k) Larger version of two final super-resolution images for microbubble and nanodroplet experiments, respectively. All images were normalized so that the peak brightness equals one.

droplets as the acoustic pressure is selected to only activate the largest most easily activated droplets. These activated droplets will generate acoustic signals until the next imaging pulse. The following imaging pulses will serve three purposes: first to generate images, second to destroy most of the existing microbubbles that were activated by the previous pulse, and third to activate a new subgroup of droplets. This continuous imaging, activation, and destruction can provide different localizations of multiple subgroups of activated droplets within the vessels.

The sparse and stochastic activation of the OFP droplets and the destruction of the OFP microbubbles may be due to a number of factors. A key factor is that the droplet population consists of droplets with a statistical distribution of different sizes and shell properties. The size distribution of nanodroplet can be seen from Fig. 2(b): the nanodroplets are polydisperse and their diameters are from about 50 to 350 nm. The droplet size, gas content, and shell properties are important factors determining the acoustic pressure threshold required for activating the droplets. The activation threshold of nanodroplets has been studied by many researchers and there are several theories that can explain these phenomena under different circumstances [28], [29]. The larger droplets can be acoustically vaporized more easily at a relatively low pressure as the activation threshold is inversely proportional to the diameter of the droplet. Therefore, only a sparse subgroup of relatively large droplets randomly spatially distributed in the tube is sensitive to the low activation pressure. The subsequent imaging pulse will cause a large percentage of activated nanodroplets to be destroyed, including through shell rupture,

diffusion, and dissolution [30]. The activation of nanodroplets by the next pulse may be affected by a number of factors. First, these nanodroplets may be affected by any remaining nearby microbubbles generated by the previous pulse—the wave emitted from a generated bubble could be directional and have a random direction, and therefore, a nanodroplet experiencing this wave in addition to the second pulse is likely to be activated more easily. Second, they may be affected by any increase in local thermal energy or acoustic power due to the imaging pulses, as the nanodroplets have a lower activation threshold in total when temperature or pressure increases [31]. Moreover, the nonlinear distorted wave from nonlinear propagation and from generated bubbles may also have superharmonics with a wavelength close to the diameter of the droplet; therefore, contributing to the initiation of droplet activation by the next pulse [29]. Further studies are required to determine which of these effects dominates and if other mechanisms are involved.

C. Quantification of Contrast Signals

Fig. 12 shows that when the high-frame-rate plane-wave imaging is on, the contrast signal from microbubbles within the cross-tube decreases during the first few milliseconds due to the high acoustic pressure (MI = 0.76). The normalized contrast signal from the water experiment did not change with time. For the contrast signal of nanodroplets within the crossed-tube, it gradually increased and reached plateau after about 100 ms. One possible reason for this increase may be due to the accumulation of activated droplets that are not completely disrupted by the plane waves. Another
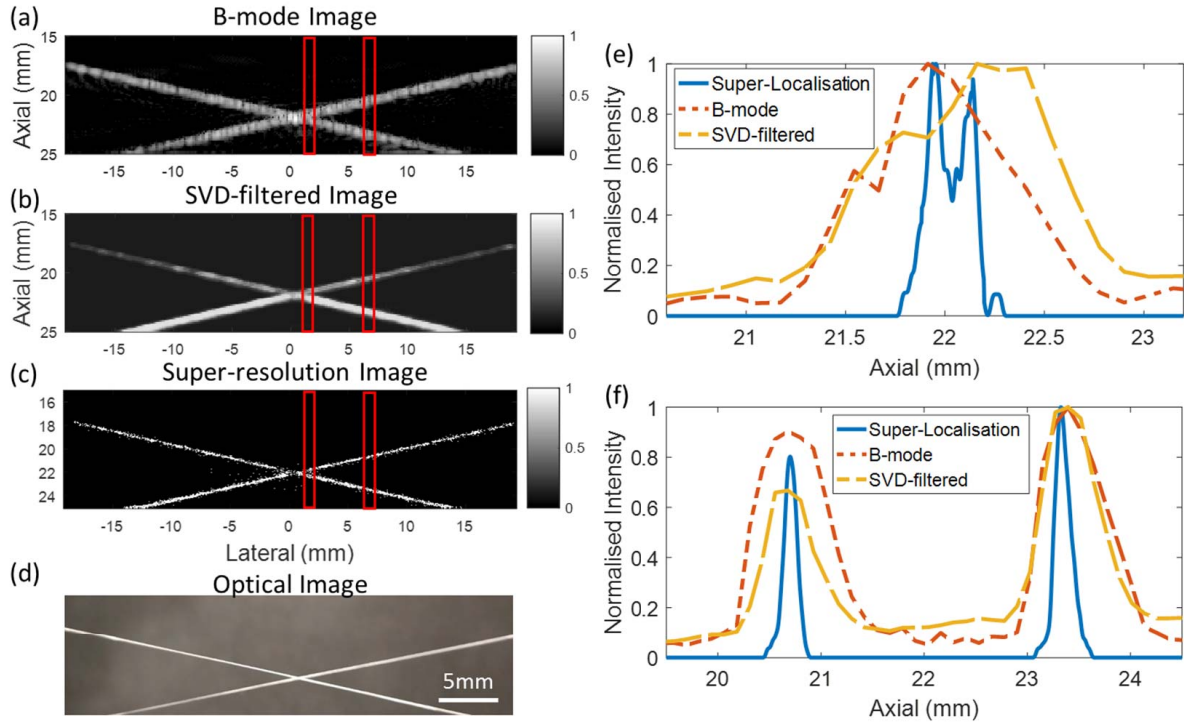
Fig. 11. (a) Conventional B-mode image. (b) SVD-filtered image. (c) Super-resolution image. (d) Optical image of the 200-μm cross-tube phantom. (e) and (f) Resolution measurements at different lateral ROIs indicated by the red lines on the images. The scale bar in the optical image is 5 mm.
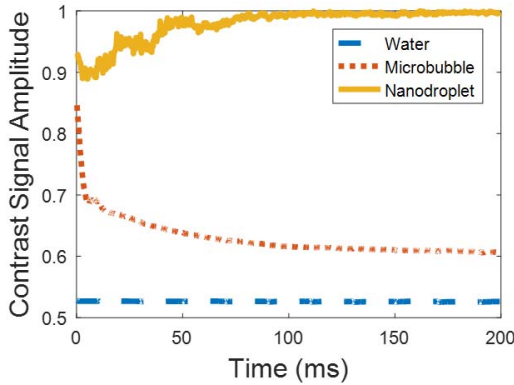

Fig. 12. Quantification of contrast signal amplitude in the B-mode images for each set of experiments as a function of acquisition time.

possible reason may be that only a sparse subgroup of the OFP nanodroplets was activated by the first few plane-wave pulses. The subsequent plane-wave pulses may simultaneously deactivate the existing activated droplets and activate the unactivated droplets. It has been found that any remaining nearby activated nanodroplets generated by the previous activation may lower the activation threshold for the next activation [32]. Therefore, the nanodroplets experiencing the later plane-wave pulses will be likely to be activated more easily, thus more contrast signals can be seen at the later stage.

D. Effect of Temperature

The experiments were performed at four different temperatures ranging from 18 °C to 37 °C. As can be seen from Fig. 7, the number of localization events decreases when the temperature is 18 °C or 37 °C. The optimum temperature is likely to be around 24 °C according to the suggested results. A relatively higher temperature would lead to a lower acti-

vation threshold of nanodroplets, thus increasing the number of localization events. However, a higher temperature will also lead to more spontaneous vaporization of nanodroplets prior to acoustic activation. Therefore, there is a compromise between the ease of activation and the stability of nanodroplets.

The experiments were performed at 24 °C in order to achieve relatively optimal performance. The OFP nanodroplets can still be activated at 37 °C, as shown in Fig. 9, although fewer localization events can be obtained. In an *in vivo* situation of 37 °C, a significant portion of the OFP nanodroplets are likely to spontaneously vaporize. However, it is still feasible to use the OFP nanodroplets at 37 °C and perform *in vivo* ultrasound imaging since this has been demonstrated by a previous *in vivo* study [33]. Spontaneously vaporized OFP nanodroplets would not be an issue in fast-AWSALM as they either get deactivated by the pulses or contribute to the signal if they are not destroyed.

E. Effect of Mechanical Index

The experiments were performed using plane-wave pulses at three different MIs (MI = 0.55, 0.66, and 0.76). The results suggested that, at the highest MI, the largest number of total localization events can be obtained. The input voltage was set at 45 V in order to achieve MI of 0.76 at an imaging frequency of 3.5 MHz according to the hydrophone calibration. The transducer used needs to be operated below 50 V in order to avoid damage. Therefore, an MI of 0.76 was chosen for the experiment as the maximum which could be achieved practically. The amplitude can be reduced further through the optimization of the droplet chemistry and ultrasound pulse sequence. The depth of interest in this study is about 2–3 cm; therefore, how the technique work in deeper tissues will need to be studied further.

F. Potential Applications

This study takes advantage of the high temporal resolution of high-frame-rate imaging and the low activation threshold of the OFP nanodroplets to perform faster super-resolution imaging than previously demonstrated. The homemade OFP nanodroplets solution has the same composition as the commercial Definity©microbubble contrast agents [34]. This means that the condensation of Definity©microbubble contrast agents to nanodroplet solution can be used with this technique for preclinical *in vivo* experiments in the future and could facilitate the clinical translation of super-resolution ultrasound imaging.

V. CONCLUSION

In summary, fast-AWSALM was developed to generate super-resolution ultrasound images in hundreds of milliseconds, orders of magnitude faster than some existing ultrasound localization microscopy techniques. We demonstrate that the high-frame-rate plane-wave pulses can be used to continuously activate and destroy the OFP nanodroplets while imaging on the timescale of milliseconds to super-resolve microstructures that cannot be resolved in the conventional B-mode image, without the requirement of flow. The much smaller size of the nanodroplets compared to microbubble contrast agents means the technique can potentially super-resolve structures beyond the reach of the current microbubble-based ultrasound super-resolution approaches.

REFERENCES

[1] O. Couture, B. Besson, G. Montaldo, M. Fink, and M. Tanter, "Microbubble ultrasound super-localization imaging (MUSLI)," in *Proc. IEEE Int. Ultrason. Symp.*, Oct. 2011, pp. 1285–1287.

[2] Y. Desailly, O. Couture, M. Fink, and M. Tanter, "Sono-activated ultrasound localization microscopy," *Appl. Phys. Lett.*, vol. 103, no. 17, 2013, Art. no. 174107.

[3] O. M. Viessmann, R. J. Eckersley, K. Christensen-Jeffries, K. Tang, and C. Dunsby, "Acoustic super-resolution with ultrasound and microbubbles," *Phys. Med. Biol.*, vol. 58, no. 18, pp. 6447–6458, 2013.

[4] M. A. O'Reilly and K. Hynynen, "A super-resolution ultrasound method for brain vascular mapping," *Med. Phys.*, vol. 40, no. 11, Nov. 2013, Art. no. 110701.

[5] K. Christensen-Jeffries, R. J. Browning, M. X. Tang, C. Dunsby, and R. J. Eckersley, "In vivo acoustic super-resolution and super-resolved velocity mapping using microbubbles," *IEEE Trans. Med. Imag.*, vol. 34, no. 2, pp. 433–440, Feb. 2015.

[6] C. Errico *et al.*, "Ultrafast ultrasound localization microscopy for deep super-resolution vascular imaging," *Nature*, vol. 527, no. 7579, pp. 499–502, 2015.

[7] J. Brown, K. Christensen-Jeffries, S. Harput, C. Dunsby, M. X. Tang, and R. J. Eckersley, "Investigation of microbubble detection methods for super-resolution imaging of microvasculature," in *Proc. IEEE Int. Ultrason. Symp. (IUS)*. Sep. 2017, pp. 1–4.

[8] P. Song *et al.*, "Improved super-resolution ultrasound microvessel imaging with spatiotemporal nonlocal means filtering and bipartite graph-based microbubble tracking," *IEEE Trans. Ultrason., Ferroelectr., Freq. Control*, vol. 65, no. 2, pp. 149–167, Feb. 2018.

[9] K. Christensen-Jeffries *et al.*, "Microbubble axial localization errors in ultrasound super-resolution imaging," *IEEE Trans. Ultrason., Ferroelectr., Freq. Control*, vol. 64, no. 11, pp. 1644–1654, Nov. 2017.

[10] S. Harput *et al.*, "Two-stage motion correction for super-resolution ultrasound imaging in human lower limb," *IEEE Trans. Ultrason., Ferroelectr., Freq. Control*, vol. 65, no. 5, pp. 803–814, May 2018.

[11] D. Ackermann and G. Schmitz, "Detection and tracking of multiple microbubbles in ultrasound B-mode images," *IEEE Trans. Ultrason., Ferroelectr., Freq. Control*, vol. 63, no. 1, pp. 72–82, Jan. 2016.

[12] K. Christensen-Jeffries, J. Brown, P. Aljabar, M. Tang, C. Dunsby, R. J. Eckersley, "3-D *in vitro* acoustic super-resolution and super-resolved velocity mapping using microbubbles," *IEEE Trans. Ultrason., Ferroelectr., Freq. Control*, vol. 64, no. 10, pp. 1478–1486, Oct. 2017.

[13] F. Lin, S. E. Shelton, D. Espíndola, J. D. Rojas, G. Pinton, and P. A. Dayton, "3-D ultrasound localization microscopy for identifying microvascular morphology features of tumor angiogenesis at a resolution beyond the diffraction limit of conventional ultrasound," *Theranostics*, vol. 7, no. 1, pp. 196–204, 2017.

[14] T. Opacic *et al.*, "Motion model ultrasound localization microscopy for preclinical and clinical multiparametric tumor characterization," *Nature Commun.*, vol. 9, no. 1, 2018, Art. no 01527.

[15] O. D. Kripfgans, J. B. Fowlkes, D. L. Miller, O. P. Eldevik, and P. L. Carson, "Acoustic droplet vaporization for therapeutic and diagnostic applications," *Ultrasound Med. Biol.*, vol. 26, no. 7, p. 1177–1189, 2000.

[16] P. S. Sheeran, J. D. Rojas, C. Puett, J. Hjelmquist, C. B. Arena, and P. A. Dayton, "Contrast-enhanced ultrasound imaging and *in vivo* circulatory kinetics with low-boiling-point nanoscale phase-change perfluorocarbon agents," *Ultrasound Med. Biol.*, vol. 41, no. 3, pp. 814–831, 2015.

[17] G. Zhang *et al.*, "Acoustic response of targeted nanodroplets post-activation using high frame rate imaging," in *Proc. IEEE Int. Ultrason. Symp. (IUS)*. Sep. 2017, pp. 1–4.

[18] G. Zhang *et al.*, "Acoustic wave sparsely activated localization microscopy (AWSALM): Super-resolution ultrasound imaging using acoustic activation and deactivation of nanodroplets," *Appl. Phys. Lett.*, vol. 113, no. 1, 2018, Art. no. 014101.

[19] G. Zhang *et al.*, "Super-localisation ultrasound imaging using sparse activation of low-boiling-point nanodroplets," in *Proc. 23rd Eur. Symp. Ultrasound Contrast Imag.*, Oct. 2018, pp. 1–9.

[20] G. P. Luke, A. S. Hannah, and S. Y. Emelianov, "Super-resolution ultrasound imaging *in vivo* with transient laser-activated nanodroplets," *Nano Lett.*, vol. 16, no. 4, pp. 2556–2559, 2016.

[21] V. Hingot *et al.*, "Subwavelength far-field ultrasound drug-delivery," *Appl. Phys. Lett.*, vol. 109, no. 19, 2016, Art. no. 194102.

[22] S. Lin, G. Zhang, C. H. Leow, O. T. Matsunaga, and M.-X. Tang, "Vaporising phase change ultrasound contrast agent in microvascular confinement," in *Proc. IEEE Int. Ultrason. Symp. (IUS)*, Sep. 2016, pp. 1–4.

[23] S. Lin *et al.*, "Imaging of vaporised sub-micron phase change contrast agents with high frame rate ultrasound and optics," *Phys. Med. Biol.*, vol. 63, no. 6, 2018, Art. no. 065002.

[24] T. O. Matsunaga *et al.*, "Phase-change nanoparticles using highly volatile perfluorocarbons: Toward a platform for extravascular ultrasound imaging," *Theranostics*, vol. 2, no. 12, pp. 1185–1198, 2012.

[25] S. Lin, G. Zhang, C. H. Leow, and M. X. Tang, "Effects of microchannel confinement on acoustic vaporisation of ultrasound phase change contrast agents," *Phys. Med. Biol.*, vol. 62, no. 17, pp. 6884–6898, 2017.

[26] C. A. Sennoga *et al.*, "On sizing and counting of microbubbles using optical microscopy," *Ultrasound Med. Biol.*, vol. 36, no. 12, pp. 2093–2096, 2010.

[27] G. Montaldo, M. Tanter, J. Bercoff, N. Benech, and M. Fink, "Coherent plane-wave compounding for very high frame rate ultrasonography and transient elastography," *IEEE Trans. Ultrason., Ferroelectr., Freq. Control*, vol. 56, no. 3, pp. 489–506, Mar. 2009.

[28] P. S. Sheeran, T. O. Matsunaga, and P. A. Dayton, "Phase change events of volatile liquid perfluorocarbon contrast agents produce unique acoustic signatures," *Phys. Med. Biol.*, vol. 59, no. 2, pp. 379–401, 2014.

[29] O. Shpak, O. Verweijx, H. J. Vos, N. de Jong, D. Lohse, and M. Versluis, "Acoustic droplet vaporization is initiated by superharmonic focusing," *Proc. Natl. Acad. Sci.*, vol. 111, no. 5, pp. 1697–1702, 2014.

[30] N. Y. Rapoport, A. L. Efros, D. A. Christensen, A. M. Kennedy, and K. H. Nam, "Microbubble generation in phase-shift nanoemulsions used as anticancer drug carriers," *Bubble Sci. Eng. Technol.*, vol. 1, nos. 1–2, pp. 31–39, 2009.

[31] P. S. Sheeran and P. A. Dayton, "Improving the performance of phase-change perfluorocarbon droplets for medical ultrasonography: Current progress, challenges, and prospects," *Scientifica*, vol. 2014, Jun. 2014, Art. no. 579684.

[32] P. S. Sheeran, T. O. Matsunaga, and P. A. Dayton, "Phase-transition thresholds and vaporization phenomena for ultrasound phase-change nanoemulsions assessed via high-speed optical microscopy," *Phys. Med. Biol.*, vol. 58, no. 13, pp. 4513–4534, 2013.

[33] S. A. Choudhury, F. Xie, P. A. Dayton, and T. R. Porter, "Acoustic behavior of a reactivated, commercially available ultrasound contrast agent," *J. Amer. Soc. Echocardiogr.*, vol. 36, no. 2, pp. 189–197, 2016.

[34] P. S. Sheeran, K. Yoo, R. Williams, M. Yin, F. S. Foster, and P. N. Burns, "More than bubbles: Creating phase-shift droplets from commercially available ultrasound contrast agents," *Ultrasound Med. Biol.*, vol. 43, no. 2, pp. 531–540, 2016.

Authors' photographs and biographies not available at the time of publication.